Available online at www.sciencedirect.com
ScienceDirect
Acta Materialia 55 (2007) 6322–6330
Acta MATERIALIA
www.elsevier.com/locate/actamat

An experimental investigation of crack initiation in thin sheets of nitinol

S. Daly *, A. Miller, G. Ravichandran, K. Bhattacharya

Division of Engineering and Applied Science, California Institute of Technology, Pasadena, CA 91125, USA

Received 18 April 2007; accepted 18 July 2007
Available online 21 September 2007

Abstract

An experimental investigation into the fracture properties of 160-μm-thick edge-cracked specimens of austenitic nickel–titanium (nitinol) under uniaxial tension is presented. Using the *in situ* optical technique of digital image correlation (DIC), strain fields directly relating to phase boundary nucleation and propagation of fracture samples were observed for the first time. The shape and size of the saturation and transformation zones as a function of loading near the crack tip were examined. An average plane strain crack initiation fracture toughness (K_C) of 51.4 ± 3.6 MPa $\sqrt{m}$ for fine grained polycrystalline nitinol sheets at room temperature was measured. The extent and nature of the phase transformation obtained from DIC, combined with the relatively high value of K_C, underscores the importance of crack tip shielding in the fracture of shape memory alloys.

Keywords: Phase transformation; Shape-memory alloys; Fracture

1. Introduction

Shape-memory alloys (SMA) have the ability to return to a previously defined shape when heated past a set transformation temperature following deformation. Many SMA also display superelastic or pseudoelastic behavior, where large deformation can be recovered upon unloading. These properties make SMA and, in particular, the nearly equiatomic nickel–titanium alloy (nitinol), attractive for a variety of applications. Important among these are stents, guidewires, braided catheters and other biomedical applications, where relatively slender structures are subjected to rather complex deformations. These motivate us to understand the deformation mechanism in these materials and, in particular, the fatigue and fracture behavior. This is of great importance and concern in the medical industry where, for example, stent failure by either fatigue or fracture can cost considerable time, expense and hazard towards patients' health.

The deformation is recovered in the shape-memory effect and in superelasticity because they are accommodated by martensitic phase transformation and transformation twinning/detwinning rather than by crystallographic slip [1,2]. These materials undergo a martensitic phase transformation from a high-temperature, high-symmetry austenite state to a low-temperature, low-symmetry martensite state. The change of symmetry gives rise to multiple variants of martensite which can form transformation twins. Superelastic behavior arises when the material is deformed at a temperature T sufficiently above the transformation temperature A_f, the austenite finish temperature. The stress-induced austenite to martensite transformation gives rise to superelastic deformation on loading. However, the martensite is unstable at this temperature and transforms back to the austenite on unloading, thereby recovering the deformation. The mechanism of transformation is reasonably well understood in single crystals (see, for example, Ref. [3] and the references therein), but not completely understood in polycrystals.

Almost immediately following its development, there was significant research on the fatigue behavior of nitinol, stemming mainly from its suitability for medical applications (for e.g., see Refs. [4–7]). However, fracture of these

* Corresponding author.
E-mail address: feakins@caltech.edu (S. Daly).

1359-6454/$30.00
doi:10.1016/j.actamat.2007.07.038

alloys, an equally important issue, has received scant attention. This is partly due to the fact that high quality bulk or thin sheet specimens are not readily available. Yi and Gao [8,9] examined the fracture toughening mechanism of shape memory alloys numerically under mixed mode loading due to martensite transformation. By doing a fracture toughening analysis of SMA with a macrocrack under mixed mode loading, they saw non-symmetric transformation boundaries for both static and steadily advancing cracks, and also showed that the martensite transformation reduced crack tip energy release rate and increased toughness. Recently, numerical and finite element modeling on the fracture of nitinol has emerged due to the development of a Drucker–Prager-type constitutive model for nitinol resulting from the work of Auricchio et al. [10,11] and its numerical implementation in finite element codes such as ABAQUS. In 2005, Wang et al. [12] investigated the formation of martensite in front of cracks in pseudoelastic shape memory alloys. Using the model [10,11] for pseudoelastic nitinol, they examined the stress-induced martensitic transformations near the crack tip of a compact tension specimen. They found that the size of the martensitic and transformation zones increase with crack length, that cracks propagate into the stress-induced martensite, and that the formation of stress-induced martensite in front of the crack tip has similarities with results in plasticity. Recently, Daly et al. [21] performed a 2-D small-scale transformation analysis for a crack under plane stress in nitinol. The analysis provided a quantitative understanding of the role of phase transformation in crack tip shielding.

Although there have been recent developments in the modeling of fracture in shape memory alloys, there is a need for high-quality experimental work. Ni–Mn–Ga, a ferromagnetic shape memory alloy which is prone to fracture under thermal cycling, contrary to most SMA, is an exception. Xiong et al. [13] studied the thermally induced fracture of single crystal Ni–Mn–Ga using *in situ* optical microscopy coupled with scanning electron microscopy (SEM) observation. Shen et al. [14] used a different approach, studying cracking in a Ni_2–Mn–Ga alloy using differential interference contrast microscopy. However, these experiments were largely qualitative and performed on Ni–Mn–Ga alloys.

Experimental studies have also been performed on the shape memory alloy CuAlNi. Loughran et al. [22] conducted an experimental investigation into the fracture of single crystals of the shape memory alloy CuAlNi using a high resolution CCD camera attached to a metallurgical microscope to optically observe fracture behavior. These experiments show that details of crack growth in single crystals depend strongly on both the type of microstructure that forms and how this microstructure interacts with the growing crack. Specifically, the observed fracture behavior is strongly dependent on the structural phase transformation the material undergoes. However, as Loughran et al. note, the experiments were designed to give unconstrained microstructures. In the case of polycrystalline shape memory alloys, which are much more commonly used, intergranular constraints will be present. There is a strong need to study the effect of these constraints on the process of fracture.

In addition to the studies of Loughran et al., there have been other studies on the fracture behavior of CuAlNi shape memory alloys. Vasko et al. [23] looked at the formation of martensite near the crack tip in single crystal CuAlNi loaded in tension. The experimentally observed martensitic microstructures near the crack tip were compared with predictions from the combined stress field and the Crystallographic Theory of Martensite (CTM). It was found that this method could accurately predict the orientation, number, and order of the austenite-martensite interfaces that initially form near a crack. Shek et al. [24] experimentally determined the fracture toughness of CuAlNi single crystals, and found that the parent phase has a higher value of fracture toughness than the martensite phase due to stress-induced transformation. Lu et al. [25] studied the CuAlNi alloy by using *in-situ* microscopy to investigate the mechanism of microcrack initiation. They found that various martensite phases appeared around the notch tip on loading, followed by microcracks that initiated along the martensite/parent interface. Recent work by Crone et al. [26] discusses a combination of indentation techniques and crystallographic information obtained by Electron Backscatter Diffraction (EBSD) in order to compare observed surface features to predicted austenite-martensite interfaces, slip planes, and possible fracture planes of CuAlNi. There have been an increasing number of experimental studies utilizing indentation techniques, particularly on thin films on Nitinol (see, for example, Ref. [26] and the references therein).

In this paper, full-field measurements of the strain during stress-induced martensitic phase transformations near the crack tip of an edge-cracked specimen of a nominally 150 μm nitinol sheet under uniaxial tension are presented for the first time. These measurements were obtained using digital image correlation (DIC), an *in situ* optical method that measures displacement on the surface of an object by tracking and correlating a random pattern on the sample surface [15]. The observations show the shape of the martensite and transformation regions as well as strain distribution inside those regions. The average plain strain fracture toughness K_C for thin sheets is determined for the first time. Though some measurements can be found in a study of the effect of hydride and hydrogen-induced martensite on the fracture toughness of nickel–titanium [16], no clear value has been established to date for nitinol. Moreover, the usual set-ups for fracture toughness measurements have generally included bulk material (thickness >1 mm) with compact tension specimens or thin sheets (thickness <10 μm) using indentation methods [17]. Very few experiments have investigated the intermediate thickness range of 100 μm, which is of practical importance in biomedical applications such as stents.

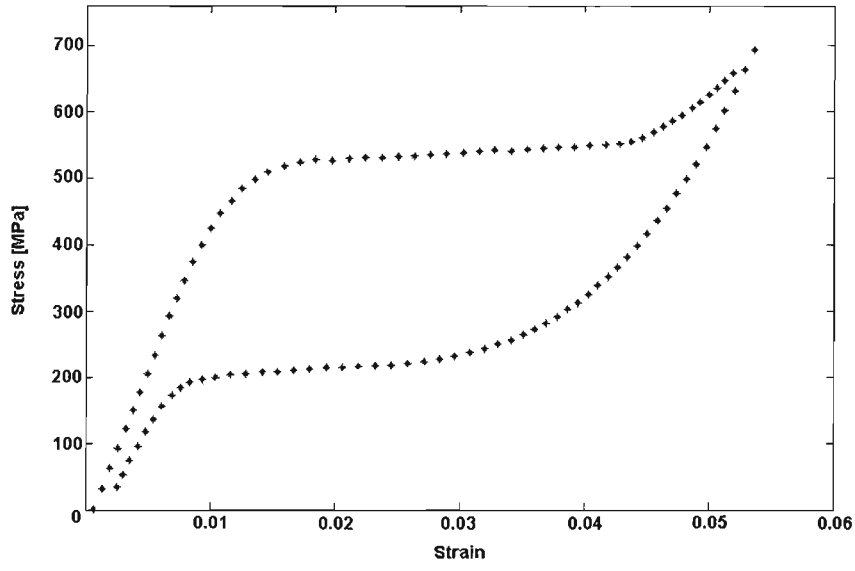

Fig. 1. Nominal (engineering) stress–strain curve for nitinol deformed in uniaxial tension at room temperature under a strain rate of $10^{-3}\,s^{-1}$.

2. Experiment

2.1. Material and specimen

Samples were cut from rolled sheets with a nominal thickness of 160 μm and composition of 52 wt.% nickel and 48 wt.% titanium. The sheets were flat annealed with an A_f temperature of 11.3 °C. The low A_f ensured that the specimens were fully austenitic when unloaded and that the stress-induced martensite occurred upon loading at room temperature. The nominal (engineering) stress–strain curve at room temperature for the nitinol material deformed at $10^{-3}\,s^{-1}$ in uniaxial tension under investigation is shown in Fig. 1 [20]. The superelastic plateau stress is around 500 MPa. The strains at the onset (austenite to martensite) and completion (fully martensite) are ~0.015 and 0.045, respectively.

Rectangular samples of 13 × 30 mm with a nominally 6-mm-long sharp edge crack were cut parallel to the rolling direction (RD) of the sheet. The specimen geometry of the edge-cracked panel and the idealized conception of various regions undergoing phase transformation for nitinol are shown in Fig. 2. In Fig. 2, x_1–x_2 are the crack tip coordinates, and a and w are the crack length and width of the specimen, respectively.

2.2. Testing

The edge-cracked specimens were tested in uniaxial tension at room temperature under displacement control using a computer-controlled servo-hydraulic machine (MTS model #358.10). Knurled grips were used to minimize slippage and were carefully aligned to minimize out-of-plane loading and displacement. Grip slippage was also minimized by attaching emery paper to the grip sections of the sample in order to maximize friction in the connection between the grips and the sample. Specimens were tested with a fixed bottom grip and moving upper grip, both of which were supported by pivots to minimize bending and shear in the specimens. The specimens were deformed at a nominal strain rate of $10^{-3}\,s^{-1}$. This is somewhat higher than the $10^{-4}\,s^{-1}$ recommended by various researchers for ideal isothermal tests, but was found to be adequate for the thin sheets and enabled a variety of observations to be recorded.

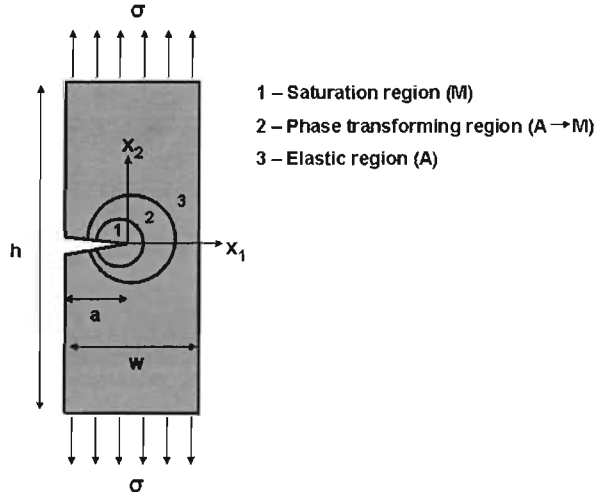

Fig. 2. Edge-cracked specimen geometry showing the coordinate system and dimensions. An idealized conception of various phase transforming zones near the crack tip is illustrated (1, martensite; 2, phase transforming zone; 3, austenite). This figure is not to scale. The actual transformation regions are much more closely confined to the crack tip.

2.3. Digital image correlation

Strain in the specimen was measured using the optical technique of DIC. This is an *in situ* optical correlation method used to measure displacement on the surface of an object by tracking a random pattern on the sample

surface. The random pattern could be inherent surface features or an artificially applied pattern, but must provide a sizeable number of correlation points at the magnification of imaging. In the present study, the pattern was applied prior to testing by first coating the sample in white paint and then using an airbrush gun to spray a light mist of black paint in a fine speckle pattern. Images were recorded using a 1200 × 1600 pixel CCD camera (Uniq Model No. UP-2000CL) focused on the specimen surface and linked to a computer for data acquisition. Between one and three telephoto lenses were used to focus the image depending on the area of interest; a Nikon AF Nikkor 50 mm *f*/1.8 was used as the main lens, and two Sigma × 2 and Sigma × 1.4 lenses were also utilized for zooming purposes. Since the deformation was in plane, a single CCD camera could be used to capture the deformation. Images were taken after each displacement increment, and post-processing was achieved with the Vic-2D software developed by Correlated Solutions [18] to extract the strain fields.

2.4. Sources of error in DIC

There are certain sources of error in these experiments that need to be discussed briefly. There is grip slippage, although testing for stability of the testing machine (MTS) applied force pre-testing helped to minimize this error. There is grip alignment error, which was minimized by carefully aligning the grips and checking the alignment in each experiment, and the self-aligning nature of the grip. There are also analysis errors due to any out-of-plane deformation of the specimen. There are numerous parameters in the Vic-2D Correlated Solutions digital correlation program that can be adjusted, and these parameters have a significant effect on the success of the correlation. Improper lighting, dust, marks on the camera lens, inadequate camera shutter speed or inadequate aperture speed can produce a faulty or blurred speckle pattern and cause failure. With their specifications and settings, the authors estimate the strain accuracy to be ~0.1%.

3. Results and discussion

The main goals of this work were to apply DIC to study the fracture of pseudoelastic shape memory alloys, provide high-quality quantitative visualization of the crack tip fields during phase transformation at the crack tip for the first time, and to determine the value of the plane strain fracture toughness K_C at room temperature for thin sheets of nitinol.

3.1. Stress intensity factor and fracture toughness

The mode-I stress intensity factor for an edge-cracked panel under uniaxial tension is,

$$K_I = f\sigma\sqrt{\pi a_{eff}} \tag{1}$$

where f is a dimensionless parameter or function dependent on specimen and crack geometry, σ is the global applied stress, and a_{eff} is the effective crack length. Since the phase transformation zone is small and confined to the region close to the crack tip, we will approximate the effective crack length to be a. The function f for an edge crack in an infinite length sheet with $\frac{a}{w} \leq 0.6$ [19] is

$$f\left(\frac{a}{w}\right) = \sec\left(\frac{\pi a}{2w}\right)\sqrt{\left(\frac{2w\tan\left(\frac{\pi a}{2w}\right)}{\pi a}\right)} \times \left[0.752 + 2.025\left(\frac{a}{w}\right) + 0.37\left(1 - \sin\left(\frac{a}{w}\right)\right)^3\right] \tag{2}$$

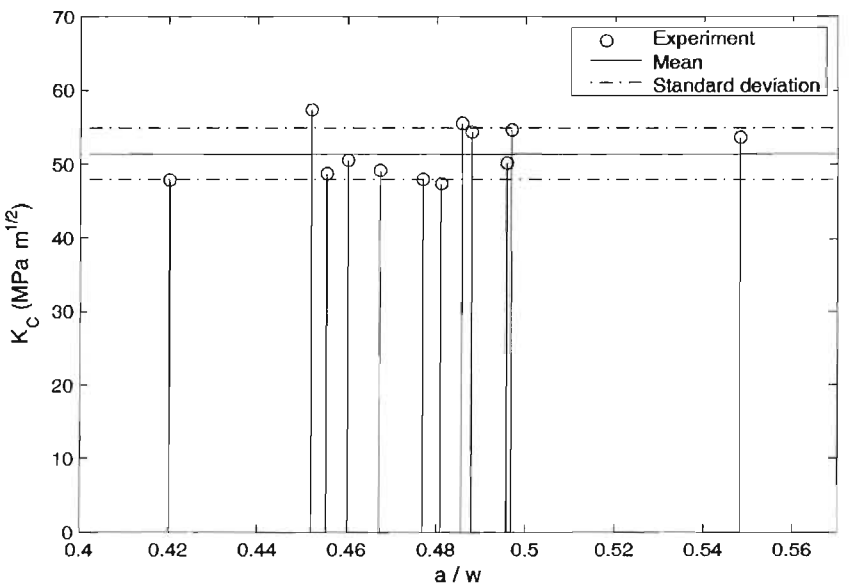

Fig. 3. Fracture toughness (K_C) values obtained for thin (~150 μm thick) sheet of nitinol using an edge-cracked specimen (see insert) for various values of (a/w).

where w is the width of the sample, which is 13 mm. Sharp edge cracks were cut into the sample before each test, and the length a was measured prior to testing. The applied stress σ was calculated by dividing the measured load by the cross-sectional area of the specimen.

Several tests with different a/w ratios were performed until failure. The maximum load was recorded and was used to compute the fracture toughness using Eq. (1). The corresponding values for the fracture toughness K_C are shown in Fig. 3. The results are independent of the ratio a/w, which is as expected. The average value of $\overline{K}_c = 51.4$ MPa $\sqrt{m}$, and the standard K_C deviation is 3.6 MPa $\sqrt{m}$.

The relatively high value of the fracture toughness in this case is attributed to the effect of phase transformation on crack tip shielding. This is supported by a recent small-scale transformation (SST) analysis of a crack in nitinol under plane stress conditions [21]. Studies on the fatigue–crack propagation behavior of nitinol conducted by McKelvey and Ritchie [4] also conclude that stress-induced martensitic phase transformation occurs in the vicinity of the crack tip for very thin superelastic austenite samples. However, in plane strain samples, McKelvey and Ritchie found that superelastic phase transformation ahead of the crack tip is suppressed, leading to a low fatigue threshold and high crack-growth rate in nitinol compared with other biomedical metallic alloys. The difference in fatigue and crack growth behavior observed in samples in plane stress vs. plane strain is a topic needing further study, especially when considering the numerous biomedical applications of nitinol devices with widely varying dimensions and states of stress.

3.2. Fracture surface

Edge-cracked fracture samples with varying orientation with respect to the RD were extracted from the same sheet and subjected to a quasi-static uniaxial tension test until failure. SEM images of the resulting fracture surfaces are shown in Fig. 4 for three specimens, oriented along the RD, 45° to the RD, and perpendicular to the RD, respectively. The fracture surfaces observed using SEM are consistent with previous experimental observations made by Daly et al. [20], where uniaxial tensile specimens aligned along the RD accommodated a significantly higher transformation strain than other textures. In Fig. 4, all images show the void growth and coalescence characteristic of ductile fracture. However, the void growth in the fracture surface of the specimen with the crack oriented along the RD shows a reduced symmetry, indicating a greater amount of shear at failure which may be due to the elongated austenite grains in the RD. The micromechanics of fracture and its dependence on texture need further investigation.

3.3. Strain fields

Two aspects of the strain field in the vicinity of the crack tip will be highlighted in the following section: the elastic field outside the phase transformation zone, and the field close to the crack tip where phase transformation (from austenite to martensite) and saturation (martensite) occur. The strain field ε_{22} is the strain along the direction normal to the crack tip. The samples used were edge-cracked specimens with nominally $a/w = 0.48$ and a nominal thickness of 160 μm, where a and w are the length of the crack and width of the specimen, respectively. The strain fields around the crack tip are characterized using the DIC technique described in Section 2.3.

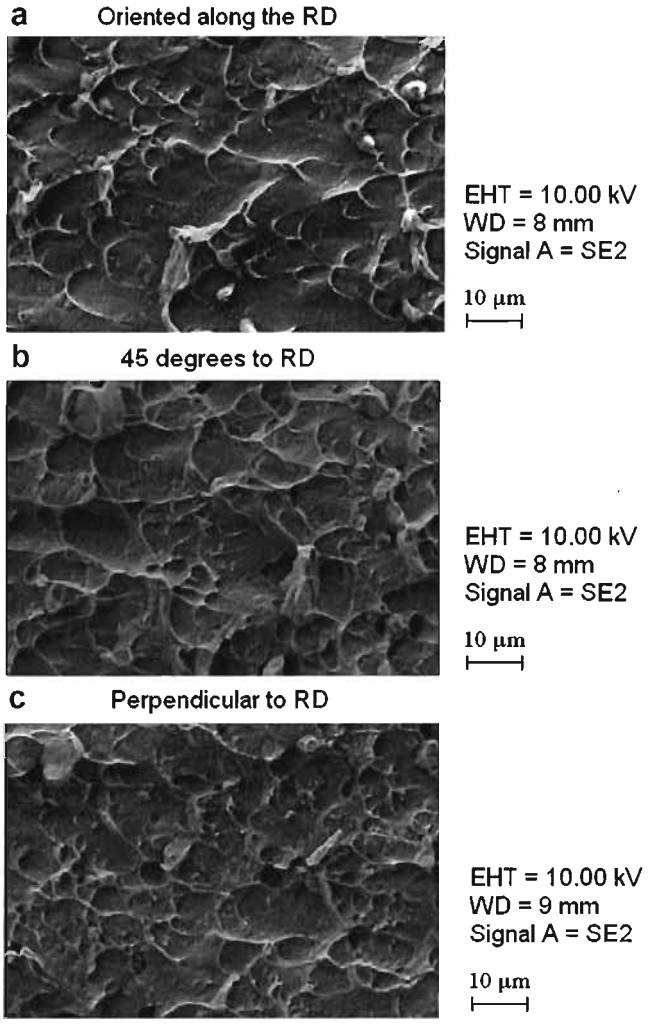

Fig. 4. Scanning electron micrographs of fracture surfaces in the vicinity of the crack tip for a crack oriented (a) along the RD, (b) 45° from the RD, and (c) perpendicular to the RD.

3.3.1. Elastic field

First, the elastic field far from the crack tip is considered. Fig. 5a–c presents a detailed progression of the fracture behavior for the edge-cracked specimen subjected to uniaxial tension under displacement control for applied $K_I = 25$, 33 and 44 MPa $\sqrt{m}$, respectively. Snapshots of the specimen were taken after each displacement increment, and the strain distributions (ε_{22}) were computed using DIC. The field of view of each image is 600 × 500 pixels (9 × 7.5 mm).

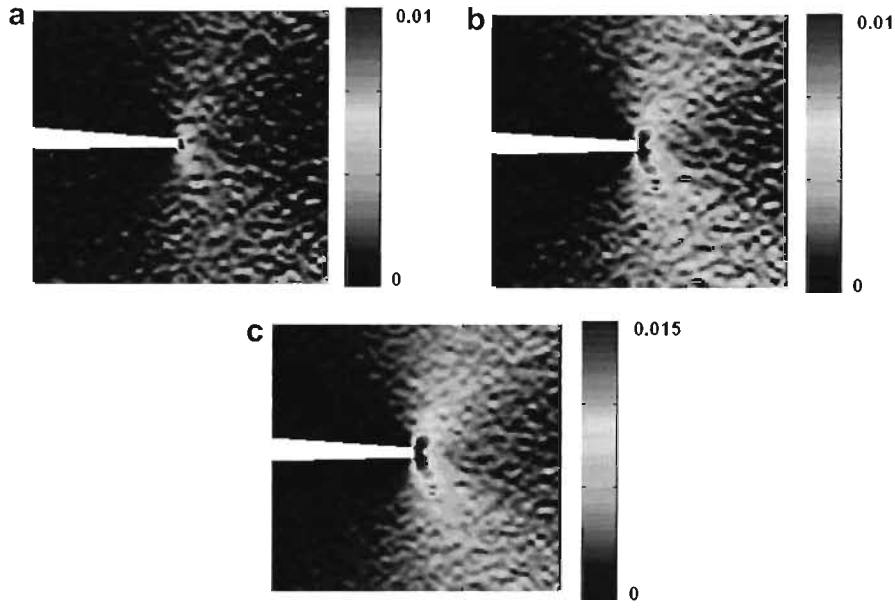

Fig. 5. Full field normal (ε_{22}) strain fields obtained using DIC in the vicinity of the crack tip for various values of applied K_I (in MPa $\sqrt{m}$) of (a) 25, (b) 33 and (c) 44. The field of view is shown in pixels (1 pixel = 0.015 mm).

In Fig. 5a, the strain field shows two inclined lobes, pointing in a direction of ~60° from the x_1-axis (crack line). The area of phase transformation and saturation near the crack tip is visible as a small lobe extending parallel to the crack tip. Phase transformation will be discussed in greater detail with higher resolution in the next section, but one should be aware that it is still present and visible at this scale. In Fig. 5b and c, the two elastic lobes grow significantly but maintain the same shape and orientation as the load increases.

Fig. 6 shows strain as a function of distance from the crack tip for various levels of the stress intensity factor. Far from the crack tip, the strain is relatively constant. As one approaches ~1.5 mm from the crack tip, one begins

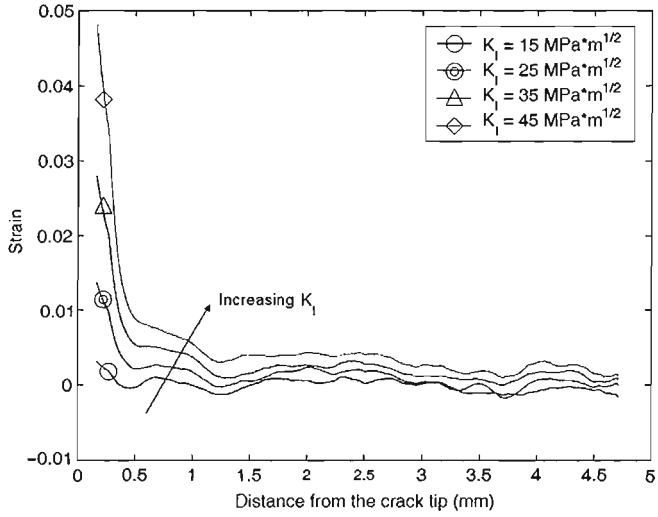

Fig. 6. Normal (ε_{22}) strain distribution along a line ahead of the crack tip at various values of applied K_I shown in the legend.

to see the $\frac{1}{\sqrt{r}}$ dependence predicted by linear elastic fracture mechanics, until $\sim x_1 \leqslant 0.3$ mm, where phase transformation begins. The actual value of strain when phase transformation and saturation begin is, of course, dependent on K_I. This dependence is discussed in the following section.

3.3.2. Phase transformation field

Fig. 7a–d presents a detailed progression of the phase transformation in the edge-cracked specimen subjected to uniaxial tension under displacement control, but at higher resolution than in Fig. 5a–c shown in the study of the much larger elastic field. Here, the strain fields are shown in a 110×50 pixel (1.6×2.2 mm) field of view centered on the crack tip, which allows the area of high stress and phase transformation immediately around the crack tip to be investigated. Snapshots of the specimen were taken at this higher magnification after each displacement increment, and the strain distributions were computed using DIC. Fig. 7a–d show the crack tip strain field for applied $K_I = 28$, 38, 47 and 51 MPa $\sqrt{m}$, respectively. Assuming that the phase transformation from austenite to martensite occurs for strains between ~1.5% and 4.5% from the stress–strain curve shown in Fig. 1, it is straightforward to track the transformation zones visually. Following this convention for transformation strain and looking along the line $\theta = 0$ and $x_1 \geqslant 0$ in Fig. 7a, there is saturation from the crack tip at $x_1 = 85$ pixels to $x_1 = 105$ pixels, when we are sufficiently far enough away from the crack tip for the strain to decrease to 4.5%. The spatial resolution of the measurements is 67 pixels mm^{-1}. Thus, the size of the saturation zone is 0.3 mm. From $x_1 = 105$ pixels, the phase transition zone extends to the right until the strain decreases to 1.5% at $x_1 = 120$ pixels, which corresponds to an additional distance of 0.2 mm past the saturation

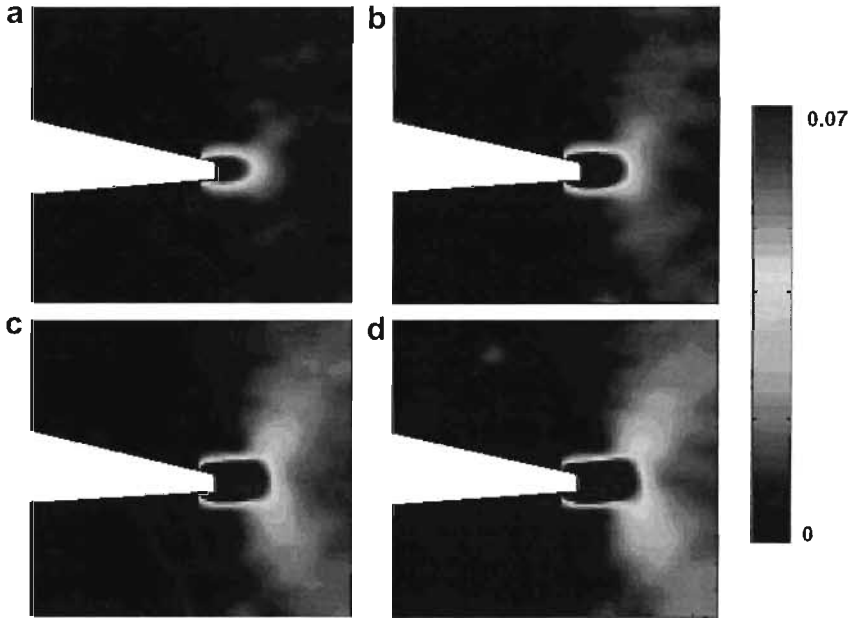

Fig. 7. Full field normal (ε_{22}) strain fields obtained using DIC in the close vicinity of the crack tip for various values of applied K_I (in MPa $\sqrt{m}$), (a) 28, (b) 38, (c) 47 and (d) 51. The field of view is shown in pixels (1 pixel = 0.015 mm). The field of view is a zoom of the region near the crack tip visualized in Fig. 5.

zone along the line ahead of the crack tip. The material is untransformed austenite for distance, $r > 0.5$ mm. At this applied level of loading K_I, the shape of the transformation zone can be viewed as a lobe that is an extension of the previously existing crack.

As K_I increases to 38 MPa $\sqrt{m}$ in Fig. 7b, the shape of the transformation zone grows longer. It still grows primarily in the x_1 direction, although there is a hint of the formation of lobes at 60° to the x_1-axis. Following the same methodology as for $K_I = 28$ MPa $\sqrt{m}$, here the saturation zone ($\varepsilon_{22} > 4.5\%$) extends to $x_1 = 0.37$ mm ($x_1 = 110$ pixels), and the transformation zone extends an additional 0.23 mm past the saturation zone along the line ahead of the crack tip. The material is untransformed austenite at $x_1 > 0.60$ mm. As K_I continues to increase in Fig. 7c and d, the transformation zone extending horizontally ahead of the crack tip continues to increase slowly in length. In addition, there is now the formation of two distinct lobes pointing 60° from the x_1-axis at the end of the horizontal transformation zone. Fig. 7c, for $K_I = 47$ MPa $\sqrt{m}$, shows the two lobes emanating from the end of this high strain region that extends parallel to the crack. In Fig. 7d, for $K_I = 51$ MPa $\sqrt{m}$, it is observed that both the region parallel to the crack and the two lobes continue to grow.

The variation in the strain field ahead of the crack tip along the x_1-axis is shown in Fig. 8. In comparison to Fig. 6, which details the nominally elastic region defined by $r \in [0,5]$ mm and $\varepsilon_{22} \in [0,0.05]$ mm, Fig. 8 details the phase transformation region defined by $r \in [0,1]$ mm and $\varepsilon_{22} \in [0,0.4]$ mm. Note that the curves in Fig. 8 have been smoothed in the post-processing algorithm, due to the large

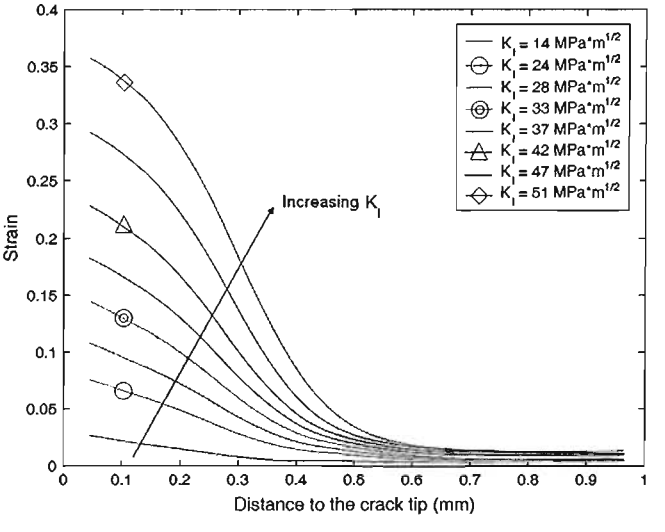

Fig. 8. Normal (ε_{22}) strain distribution as a function of distance along a line ahead of the crack tip at various levels of K_I shown in the legend.

strains and small region under investigation. The nature of the strain field in the vicinity of the crack tip can be characterized as follows.

For $x_1 > 0.5$ mm, the region is elastic, and the strain field can be adequately described by $\frac{1}{\sqrt{r}}$. The phase transformation region is $\sim 0.2 < x_1 < 0.5$ mm. The variation in the strain in this region is approximately linear.

The strain vs. distance curve changes its curvature and becomes convex for the 0.2 mm closest to the crack tip. This change in curvature and convexity could be evidence of the elastic behavior of the martensite in the fully transformed region near the crack tip.

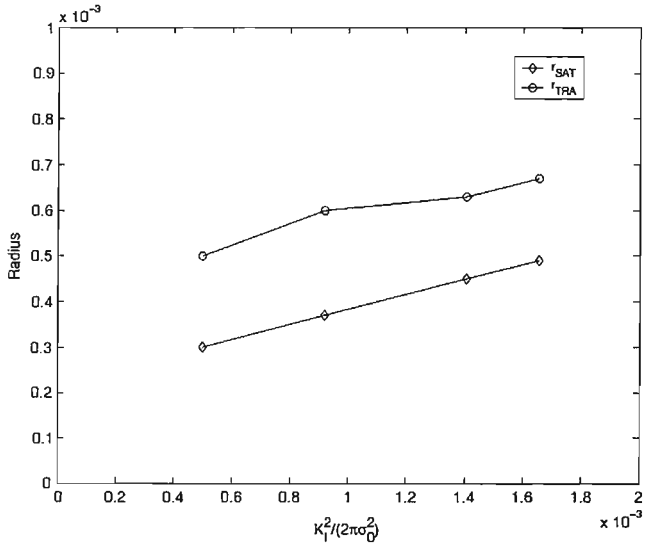

Fig. 9. Radius of the saturation zone (r_{SAT}) and phase transformation zone (r_{TRA}) as a function of $\frac{K_I^2}{2\pi\sigma_0^2}$. K_I is in MPa $\sqrt{m}$, σ_0 denotes the stress at which phase transformation begins, and is taken to be 500 MPa (see Fig. 3). The radii of the saturation and transformation zones are in meters.

The radius of the phase transforming (A → M) zone r_{TRA} and of the saturation zone (M) r_{SAT}, are plotted as functions of loading parameter $\frac{K_I^2}{2\pi\sigma_0^2}$ in Fig. 9. The loading parameter K_I is in units of MPa $\sqrt{m}$, and σ_0, the stress at which transformation begins, is taken to be 500 MPa. The zone sizes in meters are defined as the intersection of constant strain contours corresponding to 1.5% (A → M) and 4.5% (M) with the line ahead of the crack tip. The zone sizes increase linearly with the chosen loading parameter, which is consistent with the results of a recent SST analysis [21]. However, there is a change in the slope of the radius of transformation from 0.238 between $K_I = (28, 38)$ MPa $\sqrt{m}$ to 0.160 between $K_I = (47, 51)$ MPa $\sqrt{m}$. This is attributed to the formation of lobes at $K_I = 47$ MPa $\sqrt{m}$, as seen in Fig. 7c. Since the radius of the transformation zone is taken to be the intersection of the 4.5% constant strain contour with the line ahead of the crack tip, this measurement only takes into account the main lobe extending parallel to the crack tip, not the new lobes angled to the crack tip. When the new lobes appear, there is a perceived decrease in the rate of expansion of the phase transformation zone extending directly parallel to the crack tip.

Using this convention, the saturation and phase transforming zones sizes can be expressed as a function of the loading parameter

$$r_{SAT} = 0.164\frac{K_I^2}{2\pi\sigma_0^2}$$

$$r_{TRA} = 0.238\frac{K_I^2}{2\pi\sigma_0^2}$$

$$r_{TRA} = 0.160\frac{K_I^2}{2\pi\sigma_0^2}$$

It is noted that r_{TRA_C} at crack initiation ($K_I = K_C$) is ~0.3 mm, which is much smaller than the nominal crack length ($\frac{a}{r_{TRA_C}} \approx 20$) and the specimen width ($\frac{w}{r_{TRA_C}} \approx 43$). This validates the specimen design as well as the measured value of K_C under SST conditions.

4. Conclusions

This paper details the experimental investigation of martensitic transformation around the crack tip in thin sheets of Nitinol. Many applications of nitinol require its use in the form of thin sheets. One of the important failure criteria for the analysis and design of such devices is the fracture toughness, of which there are currently no recorded values for thin sheets of thickness on the order of 100 μm. Using edge-cracked specimens, an average fracture toughness (K_C) value of 51.4 ± 3.6 MPa $\sqrt{m}$ for fine-grained polycrystalline nitinol sheets ($A_f = 11.4$ °C) at room temperature was measured.

The use of DIC enabled a non-contact optical method of obtaining information about the crack tip fields in these thin sheets under displacement-controlled uniaxial tension to be used. The shape of the transformation zone can be described in the form of three lobes, one along the x_1-axis that grows larger with the load, and two lobes pointing at 60° from the x_1-axis that appear at larger values of K_I. Using the strain fields obtained from DIC, and assuming that phase transformation occurs from 1.5% to 4.5% strain, the approximate lengths of the saturation and transformation zones for various values of K_I were determined. The use of DIC enabled the first full-field quantitative mapping of the strain fields in the vicinity of the crack tip of edge-cracked specimens of nitinol. The images, combined with the relatively high value of fracture toughness for thin sheets of nitinol, indicate a complex mechanism where phase transformation contributes to toughening around the crack tip. The criteria for phase transformation and saturation near the crack tip need further investigation. The results presented here, including the full-field evolution of strain fields, could provide important insights for developing appropriate fracture criteria as well as for phase transformation under multi-axial loading conditions.

Acknowledgements

The support of the Army Research Office (W911NF-04-1-0156), the National Science Foundation (DMS-0311788) and the Powell Foundation is gratefully acknowledged. It is a pleasure to acknowledge the experimental assistance received from Petros Arakelian, Vijay Chalivendra, Tracy Kidd and Min Tao throughout this work. The authors thank Correlated Solutions, Inc. for providing the DIC correlation software (Vic-2D) used in analyzing these experiments.

References

[1] Otsuka K, Wayman CM. Mechanism of shape memory effect and superelasticity. In: Otsuka K, Wayman CM, editors. Shape Memory Materials. Cambridge: Cambridge University Press; 1998.

[2] Bhattacharya K. Microstructure of Martensite: why it forms and how it gives rise to the shape-memory effect. Oxford: Oxford University Press; 2004.

[3] Miyazaki S, Kimura S, Takei F, Muira T, Otsuka K, Suzuki Y. Scripta Mater 1983;17:1057–63.

[4] McKelvey AL, Ritchie RO. Metall Mater Trans A 2001;32(3A): 731–43.

[5] McKelvey AL, Ritchie RO. J Biomed Res 1999;47:301.

[6] Melton KN, Mercier O. Acta Metall 1979;27(1):137–44.

[7] Pelton A, Duerig T, Steckel D. Minimally Invasive Therapy Allied Technol 2004;13:218–21.

[8] Yi S, Gao S. Int J Solids Struct 2000;37(38):5315–27.

[9] Yi S, Gao S. Int J Solids Struct 2001;38(24–25):4463–76.

[10] Auricchio F, Taylor RL. Comput Methods Appl Mech Engrg 1997;143:175–94.

[11] Auricchio F, Taylor RL, Lubliner J. Comput Methods Appl Mech Engrg 1997;146:281–312.

[12] Wang XM, Wang YF, Baruj A, Eggeler G, Yue Z. Mat Sci Eng A – Struct 2005;394(1–2):393–8.

[13] Xiong F, Liu Y, Pagounis E. J Alloys Compd 2006;415:188–92.

[14] Shen LC, He JY, Su YJ, Chu W, Qiao L. Acta Metall Sin 2006;42(8):810–4.

[15] Sutton MA, Cheng MQ, Peters WH, Chao YJ, McNeill SR. Img Vis Comp 1986;4(3):143–51.

[16] He JY, Gao KW, Su YJ, Qiao LJ, Chu WY. Smart Mater Struct 2004:13.

[17] Bellante JJ, Kahn H, Ballarini R, Zorman CA, Mehregany M, Heuer AH. Appl Phys Lett 2005:86.

[18] Correlated Solutions, West Columbia, South Carolina. <www.correlatedsolutions.com>.

[19] Sih GC. Handbook of stress-intensity factors for researchers and engineers. Institute of fracture and solids mechanics. Bethlehem: Lehigh University PA; 1973.

[20] Daly S, Ravichandran G, Bhattacharya K. Stress-induced martensitic phase transformation in thin sheets of nitinol. Acta Mat 2007;55:3593–600.

[21] Daly S, Ravichandran G, Bhattacharya K. Small-scale transformation analysis of nitinol under plane stress conditions, Eng Fract Mech, in press.

[22] Loughran GM, Shield TW, Leo PH. Int. J. Solids Struct 2003;40(2):271–94.

[23] Vasko GM, Leo PH, Shield TW. J. Mech Phys Solids 2002;50(9):1843–67.

[24] Shek CH, Lin GM, Lai JKL, Tang ZF. Metall Mat Trans A 1997;28(6):1337–40.

[25] Lu YH, Qiao LJ, Chu WY. Fatigue Fract Eng Mat Struct 2002;25(5):509–18.

[26] Crone WC, Brock H. Creuziger. Exp Mech 2007;47(1):133–42.